Article

Spatial–Temporal Analysis of a Summer Heat Wave Associated with Downslope Flows in Southern Brazil: Implications in the Atmospheric Boundary Layer

Michel Stefanello [1,*], Cinara Ewerling da Rosa [2], Caroline Bresciani [3], Nicolle Cordero Simões dos Reis [1], Douglas Stefanello Facco [4], Simone E. Teleginski Ferraz [1], Nathalie Tissot Boiaski [1], Dirceu Luis Herdies [3], Otávio Acevedo [1], Tiziano Tirabassi [1], Débora Regina Roberti [1] and Gervásio Annes Degrazia [1]

1   Departamento de Física, Universidade Federal de Santa Maria, Santa Maria 97105-900, Brazil
2   Instituto Federal Farroupilha, São Vicente do Sul 97420-000, Brazil
3   Instituto Nacional de Pesquisas Espaciais, Cachoeira Paulista 12630-000, Brazil
4   Research Center on Remote Sensing and Meteorology, Universidade Federal do Rio Grande do Sul, Porto Alegre 91501-970, Brazil
*   Correspondence: michelstefanello@gmail.com

Abstract: This study investigates a summer heat wave (HW) associated with downslope winds (DWs) affecting the central region of the state of Rio Grande do Sul (RS), Brazil. The temporal evolution of both phenomena is analyzed in the atmospheric boundary layer (ABL) using a combination of micrometeorological and rawinsonde data. For spatial characterization, ERA-5 reanalysis data are used. The HW covered a large area in southern Brazil, Argentina, and Paraguay. The main features of the HW were locally enhanced in the central region of RS by the development of DWs. The establishment of DWs near the surface depends on the dynamics of the ABL and local topographic features. The results showed that DWs that occurred during the HW contributed to the extreme temperatures and were associated with strong northerly winds, low relative humidity, and a drop in the dew points. Together, these extreme events influenced the turbulent and mean flow patterns of the ABL. The increase in turbulent activity associated with the warming of the ABL favored enhanced growth of morning ABL, while at night the simultaneous effects of radiative and turbulence cooling inhibited the formation of a strong stable ABL. The analysis highlights the complex interplay of synoptic and local factors associated with DWs and HW.

Keywords: heat wave; downslope winds; regional meteorology; topography effect; atmospheric boundary layer

1. Introduction

The atmospheric boundary layer (ABL) is the lowest part of the atmosphere in which turbulent motions are ubiquitous [1]. During a daily cycle, the evolution of the ABL is generally controlled by distinct turbulent forcing mechanisms generated by local shear and buoyancy effects. The ABL is mainly governed by turbulent motions on small temporal and spatial scales that promote the exchange of scalar and vector quantities between the surface and the atmosphere. However, there are situations in which large-scale synoptic forcing (i.e., mesoscale pressure gradients, mesoscale circulations, among others) modify the turbulent generation patterns during the daily cycle of the ABL. One manifestation of this type of change in the turbulent field is provoked by topographically induced mesoscale flow [2,3]. Particularly, downslope flows are associated with strong wind and intense turbulence production [2,4–9]. Understanding downslope winds (DWs) and their interaction with turbulence are of great importance for predicting the transport and dispersion of pollutants and for developing parameterizations used in weather and climate numerical models.

DWs have been documented on different continents of the world [10]. Such flows may be associated with local intense heat episodes [11–13] and consequently promote social and

environmental impacts [14,15]. DWs are generated by large-scale synoptic conditions and interact with local terrain features on a scale ranging from the turbulent eddies to some kilometers (e.g., [16]). Such interaction can produce strong turbulence downstream [17] and alter the diurnal cycle of the atmospheric turbulent and mean variables [5,6,8,18]. Observational studies and numerical simulations of DWs have reported intense turbulence activity associated with rotors, hydraulic jumps, and gravity wave breaking [2,4,19–23]. Although many studies generally focus on high and steep mountains, idealized simulations have shown that mountain waves can also occur in more modest topography ($\approx$500 m) (see, e.g., [24]).

A less studied type of interaction concerns the coexistence of heat waves (HWs) and DWs [11,13,25–28]. From a meteorological point of view, an HW can be defined as a sustained and unusual period of elevated air temperatures [29–34]. Although progress has been made in understanding the synoptic-scale characteristics of HWs (see, e.g., [11,28,35–38], among many others), the role of ABL dynamics in this phenomenon remains poorly explored and documented. In Zhang et al. [37], the authors showed that the influence of HWs on the structure of the ABL depends on factors ranging from local to synoptic. High temperatures due to warming associated with HWs affect the development of the ABL, leading to enhanced growth of ABLs, deeper convective ABLs, and warm nocturnal residual layers [37,39]. Recently, Wang et al. [11], Turner et al. [27] and da Rosa et al. [13] have drawn attention to how downslope flows associated with HWs promote strong wind gusts and a local increase in air temperature, as well as a decrease in relative humidity, which enhances the main characteristics of HWs. Specifically, da Rosa et al. [13] showed downslope flows associated with the presence of HWs in southern Brazil during the winter season. This downslope flow, referred to as Vento Norte (VNOR, Portuguese for "North Wind"), was detected over a significant period of time during the HW phenomena. However, these concurrent events are poorly understood in the region, and little is known about their evolution and development during the summer months.

HWs have disastrous impacts worldwide, including thermal discomfort, increased mortality, wildfires, crop and livestock failures, and drought, among others [14,40–44]. HWs are one of the main consequences of global climate change, and their occurrence has increased in frequency, intensity, and duration in recent decades (IPCC, [45]). As for South America, Brazil has registered an increase in the frequency and intensity of HWs [32,33,36,46–48]. Although Brazil has continental dimensions and the climate has tropical and subtropical characteristics, there have been few studies on the characteristics and occurrence of HWs in the extreme south of Brazil.

The aim of this study is to document the summer HW case from 11 to 26 January 2022 that occurred simultaneously with a downslope flow in the central region of the state of Rio Grande do Sul (RS) in southern Brazil. An additional aim is to investigate the implication of both phenomena on the near-surface turbulence and the main features of the ABL. For this purpose, observations from a multiple-level micrometeorological tower, rawinsonde data, and ERA-5 reanalysis data were employed.

The paper is structured as follows. In Section 2, the study region and the meteorological observational data used in the analysis are presented and discussed, as well as the methodology used to identify DWs and HWs. In Section 3, a case of the simultaneous occurrence of an HW and DWs is presented and examined in terms of its spatial, vertical, and temporal structure in the ABL. Conclusions are presented in Section 4.

2. Materials and Methods

2.1. Experimental Area

The geographical area analyzed here refers to the extreme south of Brazil, as indicated in Figure 1. In particular, the focus is on the city of Santa Maria (SM), located in the center of the RS state. According to Köppen classification [49,50], the climate in southern Brazil is referred to as humid subtropical (Cfa) and is characterized by hot summers and cold winters and regular distribution of precipitation throughout the year. Typical values

for the averaged maximum temperature in the city of SM are 20.6 °C (winter; JJAS) and 30 °C (summer; DJFM) (see climate standards, Brazilian National Institute of Meteorology (INMET); https://portal.inmet.gov.br/normais accessed on 15 December 2022). According to INMET, the climate standards for January in the city of SM for the main atmospheric variables are: maximum temperature 30.9 °C, minimum temperature 19.8 °C, sea level pressure 1008.4 hPa, wind speed 2.3 ms^{-1}, and wind direction SE. The most important geographical feature of the local topography is an abrupt difference in altitude of about 400 m, which divides the relief of RS into the plateau in the north and the depression in the south (Figure 1d). The regions in the north and northeast of the depression are most characterized by the typical vegetation of the Mata Atlantica biome, while in the other regions of RS the Pampa biome predominates. The Pampa biome plays an important role in the economy of RS, as it is mainly used for activities such as livestock and agriculture.
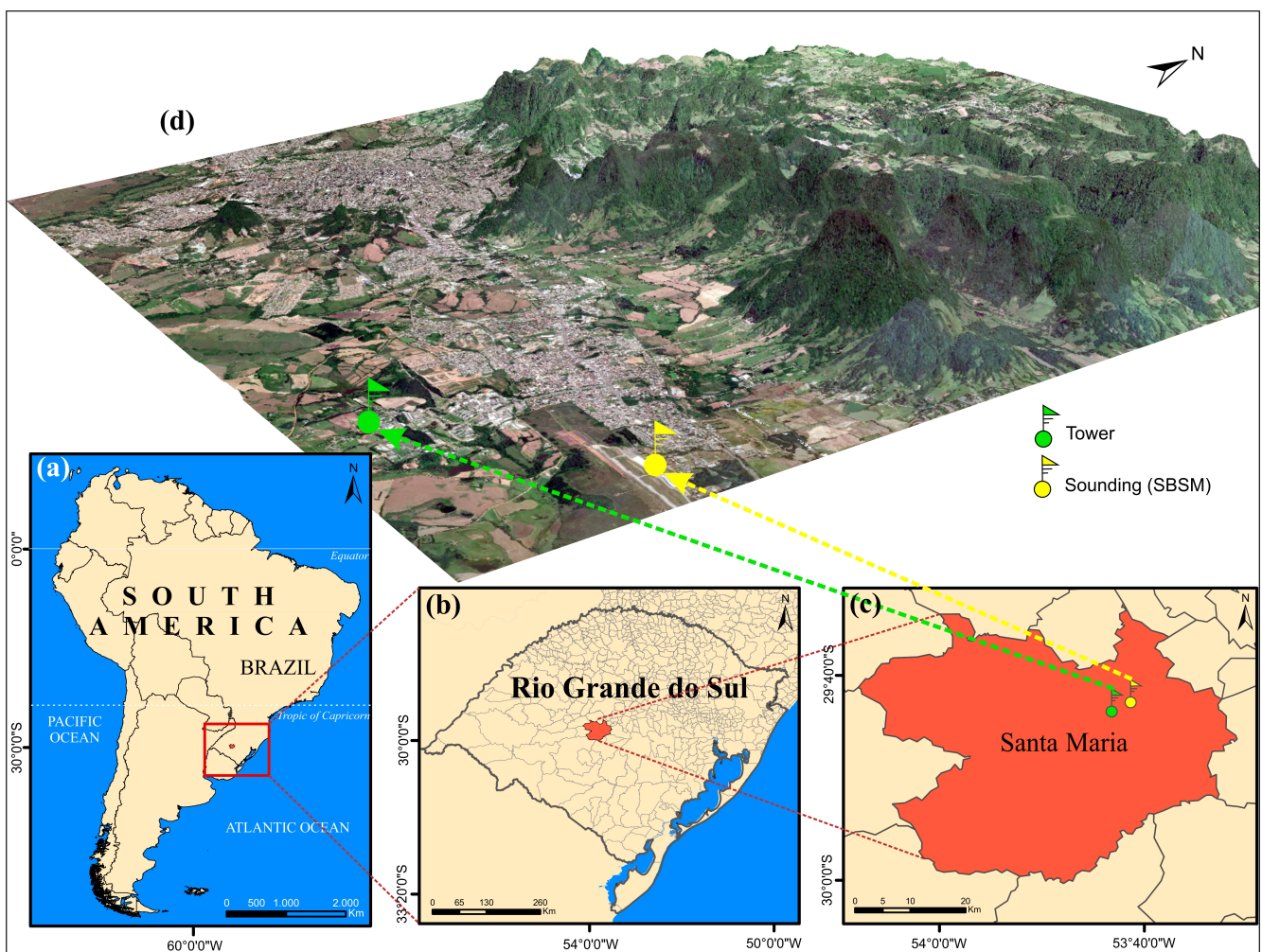

Figure 1. (**a**) Location of the state of RS in relation to South America; (**b**) position of the city of SM in RS; (**c**) location of the tower (green) and sounding on the SBSM (yellow) in relation to SM; (**d**) local topography to the north of SM.

2.2. Meteorological Observations and Reanalysis Data

The micrometeorological data used in the study were collected at a 30 m high tower (Figure 1c,d [highlighted in green]) at the Universidade Federal de Santa Maria (UFSM; RS, Brazil) experimental site (29.72° S, 53.76° W; elevation 88 m) between December 2021 and March 2022, which is the austral summer season. The tower is located in a 24 hectare area typical of the Pampa biome, characterized by low herbaceous grassland vegetation ≈8 km south of the terrain discontinuity (Figure 1). Initially, 12 levels of sonic anemometers

were installed at different heights: 1.5, 3, 5, 7, 9, 11, 14, 17, 20, 23, 26, and 30 m, and 15 levels to measure air temperature and relative humidity at 0.5, 1, 2.25, 3, 4, 6, 8, 10, 12, 15.5, 18.5, 21.5, 24.5, 28, and 29.5 m. Turbulence observations of wind components and sonic temperature were sampled at a frequency of 10 Hz, while air temperature and relative humidity were sampled each minute. Means, fluxes, variances, and other statistical moments were determined using a 30 min standard time window.

In addition to the near-surface observations, data from operational soundings conducted twice daily (near 0900 and 2100 LST; local standard time = UTC -3 h) from 14 to 18 January 2022 at Santa Maria Air Force Base (SBSM; 29.71° S, 53.69° W, elevation 85 m), located ≈3.4 km east-northeast of the micrometeorological station and ≈4 km from the terrain drop, were used to characterize the atmospheric higher levels (Figure 1c,d [highlighted in yellow]). Moreover, for the same period mentioned above, ERA-5 reanalysis data [51,52] with a spatial resolution of 0.25° × 0.25° were used to analyze the spatial behavior of the near-surface hourly atmospheric variables, such as wind (10 m), maximum air temperature (2 m) and mean sea-level pressure. Daily maximum temperature (T_{dmax}) data from 1980 to 2010 from the Climate Prediction Center (CPC; see https://www.cpc.ncep.noaa.gov/ accessed on 10 July 2022) of the National Center for Environmental Prediction (NCEP) with a spatial resolution of 0.25° × 0.25° were used to detect and characterize the HW in the area between 34° S and 24.7° S and 57.7° W and 48° W.

2.3. Identification of DW and HW

The HW episode that occurred between 11 and 26 January 2022 was detected based on the methodology proposed by dos Reis et al. [32]. Such a method considers and prioritizes the weather and climate patterns of the southern region of Brazil and eliminates the need to set arbitrary thresholds [32]. This methodology defines an HW by considering the T_{dmax} above the 90th percentile (P90) for the respective month for a period of more than 4 consecutive days. This procedure was applied to the T_{dmax} data from the CPC for the reference period 1981–2010 for the region between 34° S and 24.7° S and 57.7° W and 48° W. For this purpose, the spatial means of the daily anomalies of T_{dmax} were performed, and based on this threshold, the present HW event was defined. Specifically, the P90 threshold corresponds to 2.5 °C in the region for January. On this basis, 16 consecutive days with a maximum air temperature above this threshold were identified. During such an HW event, T_{dmax} anomalies in the southern region showed a peak on 16 January 2022 (anomalies ≈6 °C), followed by a decrease on 17–18 January 2022 and recovery on subsequent days, reaching a second peak on 22 January 2022 (anomalies ≈8 °C).

The following criteria were used to define the periods of DWs associated with an HW [13]: (i) sustained winds above 4 ms^{-1}, (ii) wind direction with a northerly component ranging from 300° (west-northwest) to 30° (north-northeast), and (iii) 4 consecutive hours meeting criteria i and ii. Based on the above criteria, 4 episodes of DW were identified. The shortest case was 4 h, and the longest was 23 h.

3. Results and Discussion

A summer HW episode that occurred from 11 to 26 January 2022 was selected as a case study because of its long duration, intensity, the influence of local topographic features on ABL formation, and impact on regional meteorological aspects. In addition, this extreme heat period had severe impacts in southern Brazil, including damage to agriculture, worsening drought, and an increase in fires [53–56].

3.1. Spatial Structure

Temperature, wind and mean sea-level pressure from the ERA-5 reanalysis data were used to explore the large-scale circulation patterns associated with the DW that occurred during the HW (Figures 2–4). The heat core of the HW was located in Argentina during 14–16 January 2022, evidenced by strong positive temperature anomalies. The large-scale patterns that favored the development of a DW in the center of RS during the period of the

HW were related to the combination of intense heat in South America associated with the South Atlantic Subtropical High near the southern region of Brazil.

At 1000 LST 14 January (Figures 2a and 3a), a high-pressure system was observed in the Argentina region (35° S, 65° W), which tended to move eastward during the next periods. A high-pressure system in Argentina was also observed by Alvarez et al. [57], during the case study of the December 2013 HW in southern South America. On the other hand, a South Atlantic Subtropical High was located near the coast of southern Brazil (center ≈ 40° W) at 1000 and 1200 LST 14 January (Figure 2b) and was associated with winds from the northern quadrant. It is noteworthy that the position of this high-pressure area was closer to the Brazilian coast than its climatological position, which varied between 30° W and 10° E in January [58]. The South Atlantic Subtropical High and the high-pressure system in Argentina resulted in a convergence region of northerly and southerly winds in Argentina, which was characterized by a temperature gradient and lower sea-level pressure.
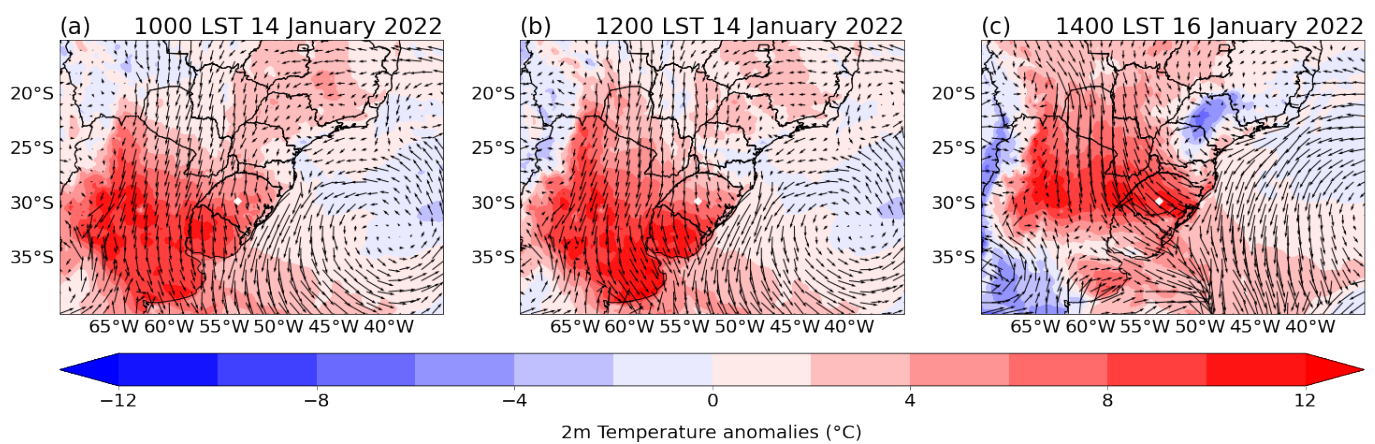

Figure 2. Maximum air temperature anomalies at 2 m and 10 m wind vectors for South America at: (**a**) 14 1000 LST; (**b**) 14 1200 LST; (**c**) 16 1400 LST; the white diamond indicates the location of the city of SM.
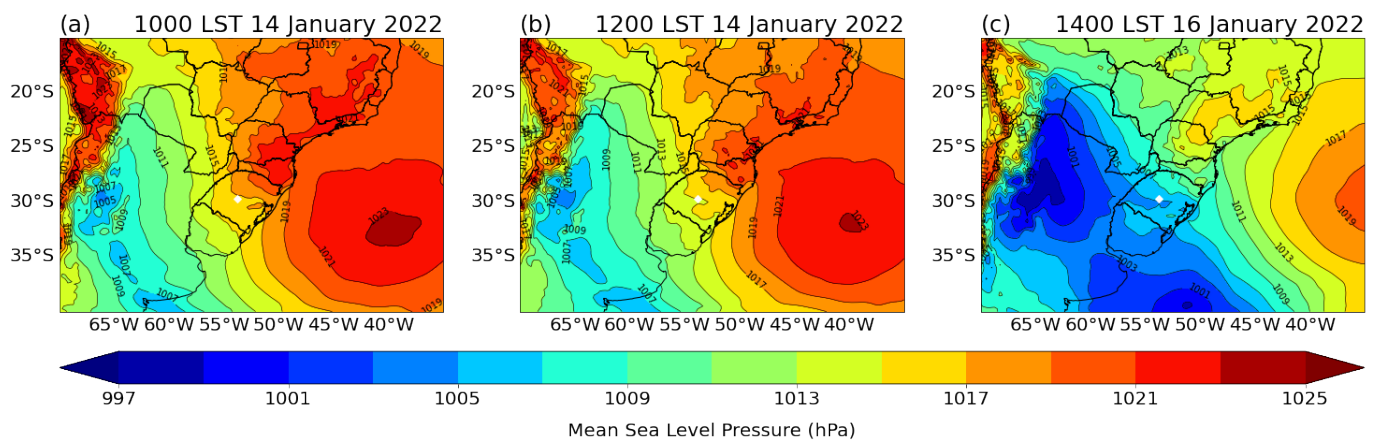

Figure 3. Mean sea-level pressure for South America at: (**a**) 14 1000 LST; (**b**) 14 1200 LST; (**c**) 16 1400 LST; the white diamond indicates the location of the city SM.

From 14 to 16 January, this temperature gradient tended to shift northward, reaching its maximum on 16 January (Figure 2c). On this last day, the convergence region was closer to the RS-Uruguay border and extended to the ocean (50° W). As the high-pressure area in the ocean moved eastward at 1400 LST 16 January (see Figures 2b,c and 3b,c), the temperature anomaly centered at SM and favored the development of strong winds from the northwest. Figure 2c shows the occurrence of a strong northwesterly low-level flow

responsible for promoting advection from the northern region, extending from southern Bolivia (20° S) to southern Brazil, ending in the convergence region in the ocean (50° W). The northerly flow at 1400 LST 16 January 2022 (Figure 3c) was associated with the lower pressure values recorded in a large part of South America. It is important to highlight that an interesting pressure pattern becomes evident when looking at RS (Figure 3c). In this case, the area of lower pressure stands out south of SM (white diamond) extending from east to west appears to follow the topographic discontinuity shown in Figure 1. This result suggests that the effects of warm advection from the north associated with terrain features were responsible for causing a local pressure drop and intensifying the pressure gradient. The flow at 10 m shown in Figures 2 and 3 is quite different from the flow at 850 hPa observed by Alvarez et al. [57]. In their case study, the flow over RS came from the east, whereas in our case the combination of the HW and advection from the northern quadrant generated the background environment that favors the development of DW in the center of RS, suggesting a coupling between these two systems. On subsequent days (17–18, not shown), the arrival of a cold front caused a change in the large-scale environment. In this case, an inversion of the wind direction occurred, shifting from the northern to the southern quadrant.

A vertical cross section of the temperature anomalies in 46° W–60° W (Figure 4) provides information about the vertical structure of the atmosphere during an HW and DW and the influence of local topography. The center of the temperature anomaly extended from the vertical layers near ≈850 hPa to the surface between 14–16 January. At 1000 LST 14 January, the center of the anomaly was at 850 hPa, while at 1400 LST 16 January it was at 925 hPa, indicating that the core of the anomalies spread from the top down into the layers near the surface. The temperature anomaly peaked at 925 hPa on day 16 at 30° S, which includes the SM region. Such a pressure level is consistent with the drop in topographic elevation located north of SM (Figure 1d). The evolution of the large-scale patterns from 14 to 16 January 2022 favored the change in winds at the ABL, promoting intense warm-air advection over nearly the entirety of Rio Grande do Sul state. The advection of warm air through the ABL was locally enhanced by local topographic features in the center of RS (around 30° S) and contributed locally to the extreme heat events.
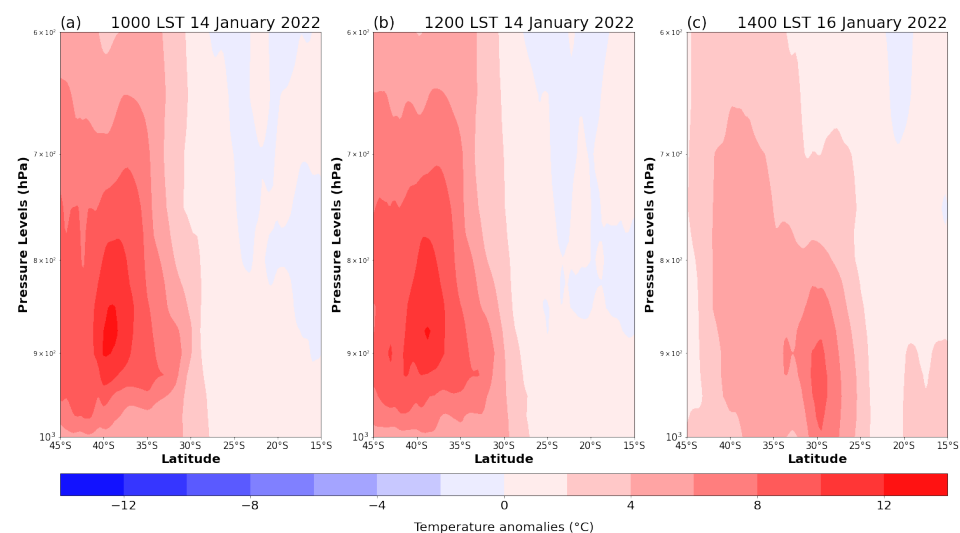

Figure 4. Latitude-height cross section in 46° W–60° W of air temperature anomalies at: (**a**) 14 1000 LST; (**b**) 14 1200 LST; (**c**) 16 1400 LST.

3.2. Temporal Structure

The time series of air temperature (Figure 5) shows a well-defined diurnal cycle from 10 to 13 January 2022. The maximum value of air temperature gradually increased from 32.2 °C (≈1700 LST) on 10 January 2022 to 36.9 °C (≈1600 LST) on 13 January 2022, and the minimum value of air temperature also increased from 17.0 °C to 19.5 °C (≈0600 LST)

during the same period. During this time interval, the mean wind speed was weak and of the order of 1.5 ms^{-1} at 3 m height. The period from 14 to 18 January 2022 (grey box in Figure 5) was characterized by the coexistence of DWs and HW. This can be seen at 0900-1600 LST on 14 January 2022 (Episode I), 2000 LST 15 January to 1900 LST on 16 January 2022 (Episode II), 0200-0800 LST on 17 January 2022 (Episode III), and 0000-0400 LST on 18 January 2022 (Episode IV) as highlighted in orange in Figure 5. The presence of DWs alters the temporal evolution of the diurnal cycle of air temperature, and it is noteworthy that the maximum values of the air temperature time series ($\approx$40 °C at 1700 LST 16 January 2022) are found when DW occurs simultaneously with an HW.

The maximum air temperature on 18 January showed lower values compared to the overall HW. This could be related to the precipitation ($\approx$10 mm) during the night from 17 to 18 January 2022. However, a recovery of the maximum air temperature values was observed on the following days. The end of the HW (26 January 2022) was characterized by a decrease in air temperature and precipitation.
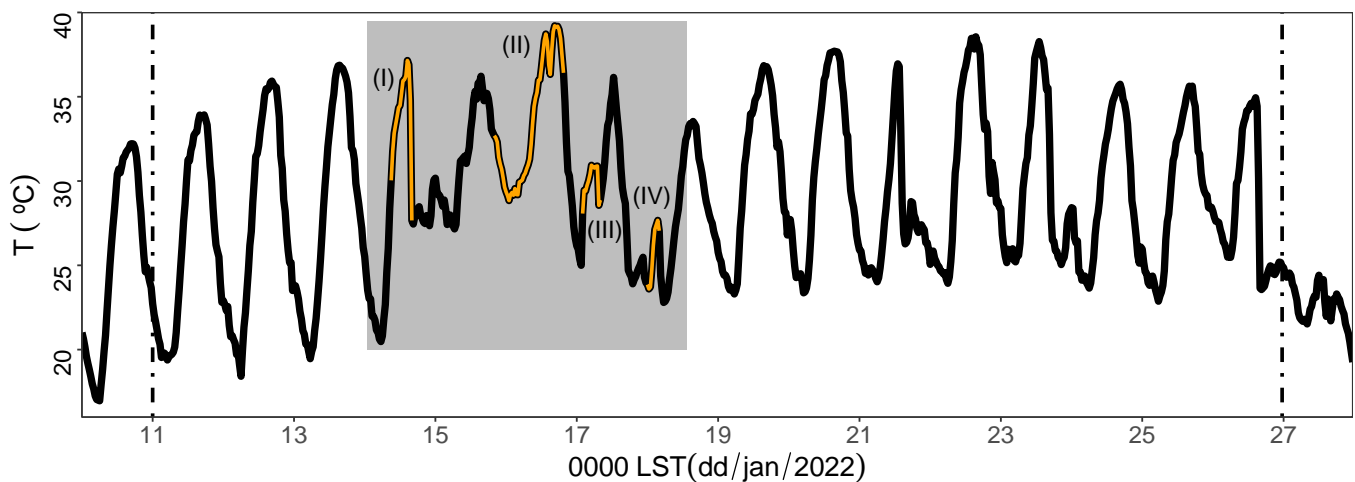

Figure 5. Time series of 3 m air temperature (*T*; black line) in the period from 10 to 27 January 2022. The orange lines highlight periods representing the DWs episodes (I–IV). The vertical dashed lines correspond to the beginning (11 January 2022) and demise (26 January 2022) of the HW, while the grey shaded area indicates the period from 14 to 18 January 2022 that was affected by the DWs.

The HW episode exhibited in Figure 5, which lasted for many days, is a good case to study the interaction between an HW, DWs, and the generation of turbulent patterns. Therefore, the period from 14 to 18 January 2022 is examined in more detail in Figures 6 and 7 and in the next section. The onset and demise of DW episodes are normally marked by abrupt changes in the local flow characteristics. In such cases, relatively high wind speeds are observed associated with a northerly wind direction component. A significant increase in wind speed persistent for about one day occurred between 2000 LST 15 January to 1900 LST 16 January 2022. In this case, the wind speed approached 6 ms^{-1} and was consistent with the observed temperature peak in the HW episode (1200 LST 16 January 2022). The intense wind speed also coincided with the low-pressure values reached during this period. Relative humidity also changed noticeably, following the opposite behavior of air temperature. During the peak of air temperature (1200 LST 16 January 2022), critical values of relative humidity were reached of the order of 25%. Relative humidity depends on both temperature and dew point. Thus, higher temperatures could lead to low values of relative humidity even if the dew point is constant, as shown in Figure 6. When DWs took place, a decrease in dew point was observed compared to the hours before and after when the dew point was nearly constant. This can be explained by the transport of dry air by a DW from higher elevations above the elevated terrain to near the surface. Therefore, the temporal variability of the dew point is an important signature of the presence of a DW.

Conditions similar to those described above have also been observed in DWs, known as Sundowners, along the coast of Santa Barbara, California [59].

The air temperature is expected to gradually decrease after sunset during the night. However, this usual behavior does not always occur during the occurrence of an HW and DW (Figure 6), as there are increases in temperature for a short time during the night, as in the nights of the 16–17 January and 17–18 January. During these periods, winds are locally enhanced by the slope of the terrain and are responsible for such air temperature behaviour.
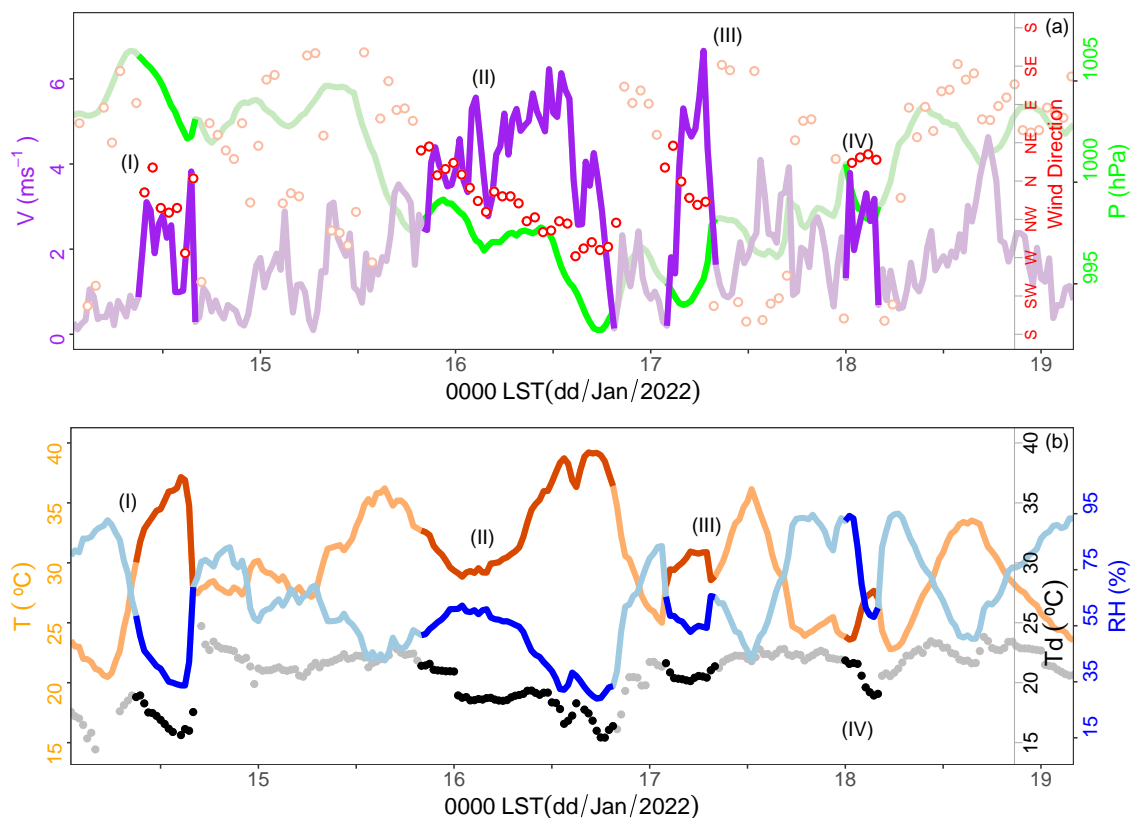

Figure 6. Time series of (**a**) wind speed (*V*; purple line), wind direction (red dots), and air pressure (*P*; green line); (**b**) air temperature (*T*; orange line), relative humidity (*RH*; blue line), and dew point (*Td*; black line) recorded during 14–19 January 2022. The highlighted periods, indicated by dark colors, represent episodes of DWs (I–IV).

Figure 7 exhibits for the same period as in Figure 6 the time evolution of the turbulent kinetic energy, $TKE = 0.5(\overline{u'^2} + \overline{v'^2} + \overline{w'^2})$, where $\overline{u'^2}$, $\overline{v'^2}$, $\overline{w'^2}$ are the velocity variance components and the sensible heat flux $H = \rho C_p(\overline{w'T'})$, where ρ is the density of air, C_p is the specific heat of air at constant pressure, and $\overline{w'T'}$ is the covariance between temperature and vertical velocity component. A greater increase in turbulent activity is observed in association with intense advection of warmer air (Figure 6). The period after the onset of a DW is characterized by an increase in TKE, which generally continues to rise in the following hours and peaks near its end. This intense turbulent regime is responsible for promoting strong turbulent mixing through the ABL. During daytime DWs, H generally exhibits large magnitudes, with a maximum mean value on the order of (341 Wm^{-2}), in contrast to the other days (280 Wm^{-2}) when only the HW occurred. Large magnitudes of H also occur during the night hours when DWs are present. Such behavior is quite distinct from the other night periods which are characterized by H near zero and low wind conditions [60]. Therefore, the analysis suggests that HW and DWs affect the turbulent fluxes and mean flow. In this sense, the DWs locally reinforce the main features of the HW, a hypothesis that is addressed in more detail in the next section.
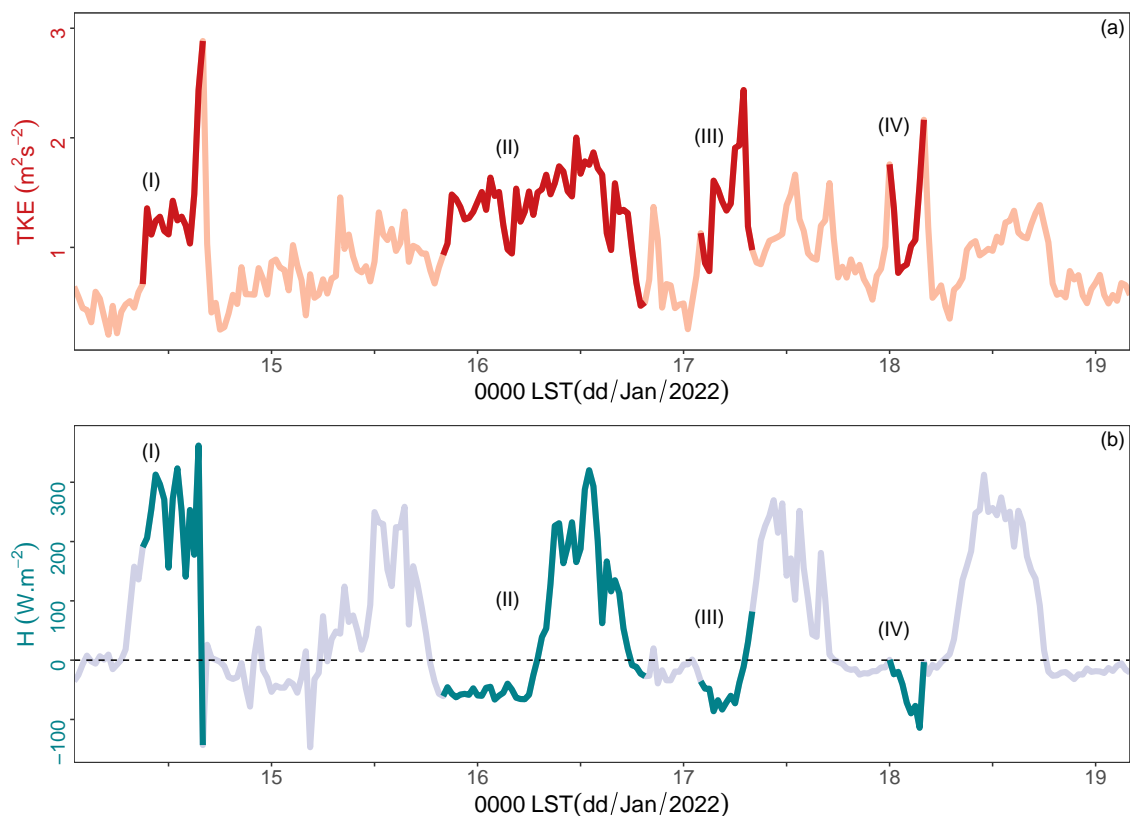
Figure 7. As shown in Figure 6, but for the: (**a**) turbulent kinetic energy (*TKE*); (**b**) sensible heat flux (*H*). The highlighted periods, indicated by dark colors, represent episodes of DWs (I–IV).

3.3. Vertical Structure

In this section, the vertical profiles of the meteorological variables are considered to obtain information on the structure of the ABL. To identify the different impacts along the ABL diurnal cycle, the profiles are divided into day and night.

Figure 8 exhibits the vertical profiles of temperature, wind speed, and direction from the atmospheric soundings. The sounding on the morning of Day 14 (0833 LST) occurred shortly before the north winds (see Figure 6a; Episode I) were detected in the near-surface layer. In this case, the wind direction was in the northern quadrant at an extensive vertical region of the ABL (Figure 8c [red line]). The wind speed profile tended to increase with height, peaking at 11 ms^{-1} at 800 m altitude (Figure 8a [red line]). At this time there was a thin unstable ABL near the surface, but above 80 m there was a transition in the potential temperature profile, which approximated to near-adiabatic profile (Figure 8b [red line]). In such a situation, there is a tendency to homogenize the temperature gradient profile. Episode I dissipated around 1600 LST on 14 January 2022 (see Figure 6). At later times, around 2100 LST, winds were weak near the surface (Figure 6a) and increased almost linearly up to an altitude of ≈400 m (Figure 8d [red line]). Above this height, the wind speed was practically constant and had strength on the order of 4 ms^{-1}. The potential temperature profile (Figure 8e [red line]) at 2031 LST shows a strongly curved profile, indicating a strong stable boundary layer and the dominance of radiative cooling processes at the surface in concordance with [60,61].

On 15 January at 0852 LST, the wind profile (Figure 8a [orange line]) was similar to 14 January at 0833 LST [red line], with a nearly constant NW direction at all vertical levels (Figure 8c [orange line]). During this period, the height of the morning ABL was on the order of 700 m (Figure 8b [orange line]), indicating a rapid deepening of the evolving convective ABL compared to the 14 January at 0833 LST [red line]. At 2000 LST on 15

January 2022, wind speed near the surface tended to increase with time to more than $2\,\text{ms}^{-1}$ (onset of Episode II; Figure 6a).

The vertical profile of wind speed (2039 LST 15 January 2022; Figure 8d [orange line]) reached its maximum ($15\,\text{ms}^{-1}$) at about 600 m altitude, blowing from a northerly direction (Figure 8f [orange line]) and weakening at higher altitudes. At the nose of the jet ($\approx$600 m), the Richardson number ($Ri_g = \frac{g}{\theta_0}\frac{\Delta\bar{\theta}\Delta z}{\Delta\overline{U}^2 + \Delta\overline{V}^2}$, where g is the gravity, $\Delta\overline{U}/\Delta z$, $\Delta\overline{V}/\Delta z$ and $\Delta\bar{\theta}/\Delta z$ are approximately the vertical of the horizontal wind velocity components and θ) reached values of 0.8, while Ri_g in the region further down and up reached values of less than 0.4 and 0.2 (not shown), respectively. The decrease in Ri_g near the surface is consistent with the intensification of winds and turbulence motions as highlighted in Figures 6 and 7. Determining the precise physics mechanism responsible for the observed behavior of the atmospheric flow variables along the manifestations of DWs is beyond the scope of this paper. However, it is interesting to mention that [24] reported the occurrence of mountain waves in modest topography (500 m) such as the one discussed here. The wind pattern observed at 2039 LST on 15 January 2022 (Figure 8d [orange line]) seems to be consistent with the development of the lee slope jet and the triggering of mountain waves. In fact, the atmospheric pressure time series at 3 m height (not shown) shows a clear oscillatory behavior during the period from 1900 to 2100 LST on 15 January 2022 and at 0300 LST on 16 January 2022. The oscillations were characterized by a time scale of 10 to 20 min, indicating a possible signature of mountain wave development. This suggests that a 30 m high micrometeorological tower may have been located in the region of turbulence caused by the wave-breaking. Therefore, this can be associated with the temperature increase, low relative humidity, dew point, and intensification of turbulent activity (Figures 6 and 7). Compared to the previous sounding (2031 LST on 14 January 2022 Figure 8e [red line]), a decrease in the curvature of the potential temperature profile was observed at 2039 LST on 15 January 2022 [orange line]. This fact is consistent with the increase in downward turbulent sensible heat flux (Figure 7b) due to the strong advection of warm air from the northern direction. Therefore, the boundary layer cooling caused by turbulence was dominant [60,61]. This indicates that the formation of a strong stable boundary layer, as indicated in the earlier night profile [red line], did not occur. This is a consequence of the turbulent activity induced mechanically by the intense northerly flow.

Sounding at 0905 LST on 16 January 2022 was launched when the DW (Episode II) at SM had already persisted for 12 h. At 0905 LST, the wind speed profile (Figure 8a [black line]) increased almost linearly with altitude reaching $\approx$20 ms^{-1} at 1200 m, in the usual height of the low-level jet [62] (see Figure 8a), and presented a well-consolidated north direction through the vertical levels. Therefore, the mechanical generation of turbulence occurred along this vertical extent. This is the case when convective forcing does not promote an effective homogenization of the wind profile. However, in a deep vertical region of the morning ABL, the potential temperature profile is nearly adiabatic (Figure 8b [black line]). Therefore, due to the robust turbulence generation, the height of the morning ABL was already 1000 m at 0905 LST. Episode II ended at 1900 LST on 16 January 2022, followed by a decrease in wind speed at the surface (see, Figure 6a). The profile of wind speed at 2038 LST on 16 January 2022 (Figure 8d [black line]) showed a maximum ($\approx$9 ms^{-1}) near 250 m. Above this level, it decreased until 700 m and then started to increase again with altitude. This behavior indicates the presence of a nocturnal low-level jet [63]. As a result, the potential temperature profile (Figure 8e [black line]) showed the presence of a shallow surface-based thermal. The wind direction profile (Figure 8f [black line]) showed two distinct patterns, one above 700 m with a wind direction from NW-N and another below 400 m with a wind direction SE-S. The height at which the wind direction changed is comparable to the elevation of the terrain to the north of the city (Figure 1d). In this case, a vertical decoupling of the flow dammed in the depression in relation to those occurring at higher altitudes can be observed. Hours later, at 0200 LST on 17 January 2022, strong northerly winds were detected near the surface (see Figure 6a; Episode III), suggesting a re-coupling of high levels to the surface. The demise of Episode III occurred at 0800 LST

on 17 January 2022, marked by a decrease in the wind speed (Figure 6a). The 17 January morning sounding (Figure 8c [light blue]) showed the presence of northerly winds in the vertical layers just above the height of 250 m. Differently, the winds were weak and of the order of 2.5 ms^{-1} in the layer between the surface and 250 m, while in the vertical layers above, the wind speed tended to increase and reached a maximum near 1400 m (Figure 8a [light blue]). The evening sounding (2041 LST on 17 January) revealed a similar wind speed profile to that observed 24 h earlier, with the wind direction also changing above the elevation of the terrain (Figure 8d,f [light blue]). The temperature profile presented lower values (Figure 8e [light blue]), which was due to the effect of precipitation in the day–night transition.

The sounding on the morning of 18 January (0840 LST; Figure 8a–c [blue line]) was launched several hours after the demise of Episode IV, which occurred at 0400 LST on 18 January (Figure 6a). The wind speed profile was similar to that of the previous day, showing low wind speed in the layer below 200 m. In this lower vertical layer, the wind comes from an easterly direction, while the profile well above takes on a northerly direction. The profile of potential temperature revealed a morning ABL of the order of 300 m. The evening vertical structure on 18 January (2043 LST; Figure 8d–f [blue line]) differed from that observed during the previous sounding, with winds assuming a near-easterly direction and not exceeding 6 ms^{-1} in the region from the surface to 500 m. The wind direction patterns indicate a change in the characteristics of the air mass that occurred at SM. The temperature profiles were also different from those observed in the previous soundings.
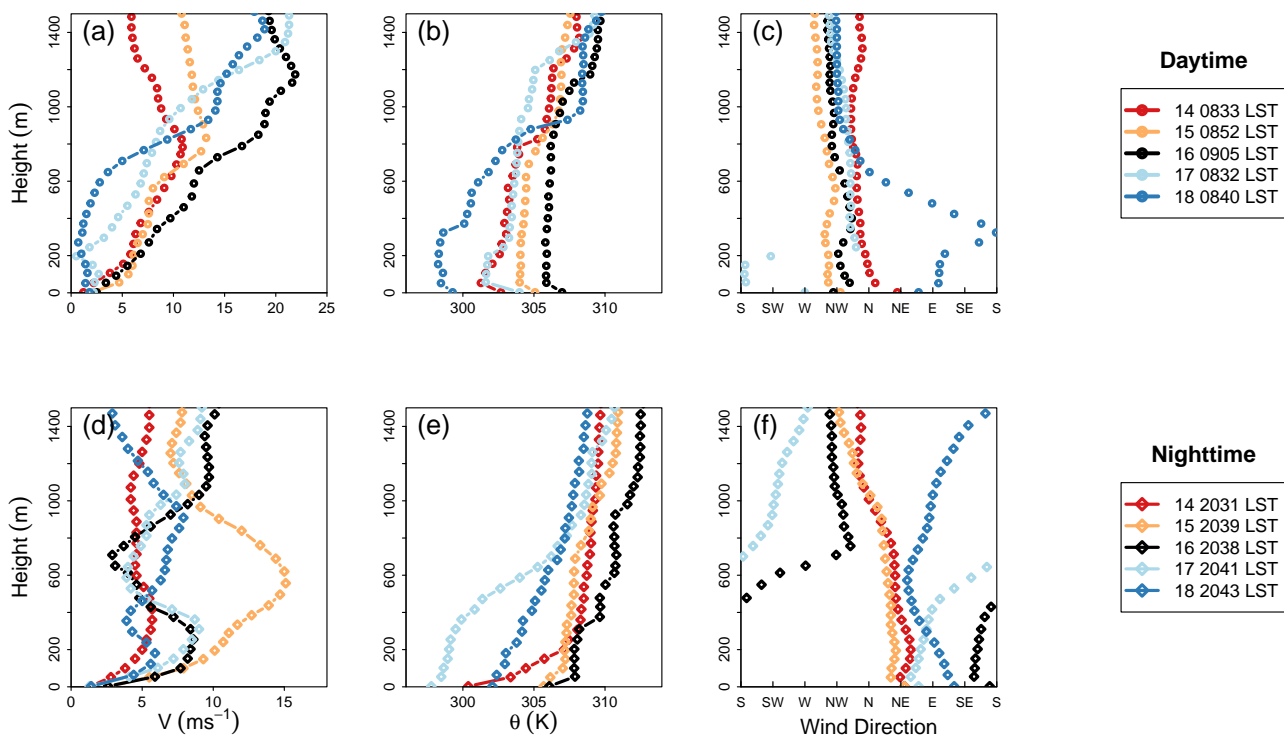

Figure 8. Vertical profiles of (**a**,**d**) wind speed (*V*), (**b**,**e**) air potential temperature (*θ*), and (**c**,**f**) wind direction during the day (top) and night (bottom) from SBSM atmospheric soundings.

Regarding Figure 8c,f, it is noteworthy that the wind direction profile exhibits a northerly component at high vertical levels, despite the near-surface levels presenting a direction that differs from the north quadrant. Although the DW was generated by a synoptic-scale environment, its development depended on surface features and dynamic processes, such as turbulence forcing mechanisms. Our results suggest that the large-scale forcing associated with an HW and local terrain features affects the growth of the morning

boundary layer and the nocturnal boundary layer by producing intense and sustained periods of warm air advection.

To examine the effects of HW and DWs on ABL flow patterns, the micrometeorological data were divided into three subgroups: (i) HW subgroup (HW_{sp}), which includes the hours of HW without the hours associated with the presence of DWs; (ii) DW subgroup (DW_{sp}), which represents the data of DWs hours that occurred simultaneously with HW; and (iii) summer subperiod (S_{sp}), which represents the data from December 2021 to March 2022 without the hours associated with the presence of HW and DWs. Figure 9 reveals three patterns in the averaged vertical profiles of wind speed, air temperature, and turbulence parameters corresponding to HW_{sp} (blue line), DW_{sp} (orange line), and S_{sp} (black line). The lowest mean wind speeds (Figure 9a,f) are found for the HW_{sp} and the highest for the DW_{sp}, while the data for the S_{sp} lie between these two. As shown in Figure 9a,f, the winds in the near-surface region are relatively weaker for HW_{sp} than for S_{sp}. Such weak airflow patterns into the ABL are abruptly modified by intermittent episodes of DWs, as shown in Figure 6. At DW_{sp}, the wind speed at 30 m height reaches values close to 6 ms^{-1}. The daytime temperature (Figure 9b,g) at 3 m height is $\approx$5 °C above the S_{sp} in the HW_{sp} and 8.5 °C above the DW_{sp}. Similar values were obtained for nighttime. It is noteworthy that the higher temperature values are associated with the strongest wind from a northerly direction and lower relative humidity. For this last variable (not shown), there is no clear difference between the data of HW_{sp} and the S_{sp}, while RH assumes low values in the DW_{sp} with a mean value of 48% for the day and 70% for the night. Therefore, DWs occurring simultaneously with an HW contribute to locally intensified heat events and to the drying of the near-surface ABL during day and night.
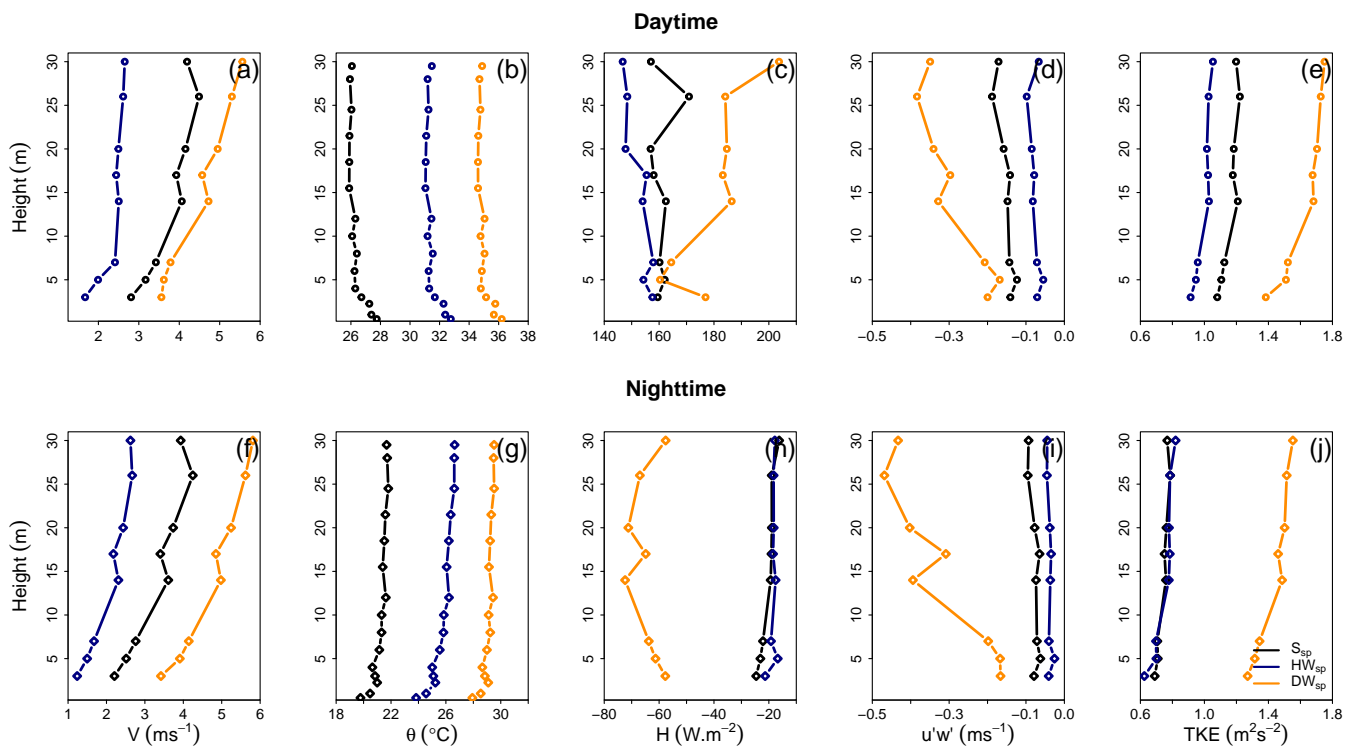

Figure 9. Vertical profiles of (**a**,**f**) wind speed (*V*), (**b**,**g**) air potential temperature (*θ*), (**c**,**h**) sensible heat flux (*H*), (**d**,**i**) momentum flux ($u'w'$), and (**e**,**j**) turbulent kinetic energy (*TKE*), for S_{sp} (black), HW_{sp} (blue), and DW_{sp} (orange); (**a**–**e**) refers to daytime, while (**f**–**j**) is for nighttime. The plots refer to the 30 m micrometeorological tower.

Figure 9c,h illustrates the intensification of the sensible heat flux (*H*) during DWs (DW_{sp}) in comparison to the other profiles. Such a profile shows positive values during the day and strongly negative values at night, which are caused by the intense advection

of warm air masses and the increased wind-shear turbulence production. The H profile is slightly lower (in magnitude) in the HW_{sp} than in the S_{sp} for both day and night conditions. The momentum flux (Figure 9d,i) increases strongly with altitude in the DW_{sp}, which is responsible for the vertical transport of momentum in the ABL. For the HW_{sp}, such a variable assumes low magnitudes compared to the other two conditions. During the day and night, the turbulent kinetic energy (TKE) is much higher for the DW_{sp} than for the HW_{sp} and S_{sp}. Although the TKE is slightly lower for HW_{sp} than for S_{sp} during the day, no clear difference was observed at night. Therefore, the interaction of DWs with the HW provides increased generation of TKE, contributing to the warming of the ABL.

4. Conclusions

This paper examines the spatio-temporal evolution of a heat have (HW) episode that occurred from 11 to 26 January 2022, simultaneously with downslope winds (DWs) at the ABL. The analysis is based on a combination of multiple-level sonic anemometer and thermo-hygrometer measurements, as well as rawinsonde data collected in southern Brazil. ERA-5 reanalysis data were also employed.

The extreme heat in Argentina and large-scale patterns associated with the HW created a background environment that favored the development of DWs along a modest declivity located north of the city of SM in the central region of the RS state. As a result, the HW episode was sometimes locally influenced by the occurrence of DWs with the longest lasting 23 h. Although a northerly wind component characterized the high layers of the atmosphere during almost all the HW manifestation period, the onset of DWs at the near-surface layers depends on the local topographic features acting on the flow as well as on the dynamics of the ABL.

The interaction of an HW and DWs influences the diurnal cycle of atmospheric forcing and consequently the evolution of the ABL. During DWs, the wind speed increased significantly compared to the entire HW episode and also to the S_{sp}. For the analyzed period, the highest temperature value was recorded of the order of 40 °C, which was associated with the simultaneous occurrence of an HW and DWs. In this extreme heat situation, relative humidity dropped to 25%, accompanied by strong winds from the north and low dew points. Compared to the S_{sp}, the temperature at the surface increased by 5 °C during the HW and by 8.5 °C during the simultaneous occurrence of the HW and DWs. Therefore, the establishment of DWs locally amplifies the main features of the HW.

The advection of warm air masses from a northerly direction enhanced turbulent activity, sensible heat flux, momentum flux, and turbulent kinetic energy both during the day and night. During the day, warming and drying of the ABL combined with strong northerly winds contributed to a significant growth of the morning convective ABL, which reached ≈1000 m in the early morning hours. At night, the strong winds combined with warm air layers did not allow the formation of a strong stable ABL presenting an accentuated surface thermal inversion. These results confirm the important role of the DWs and an HW in influencing ABL patterns, and vice versa, along the diurnal cycle.

This study highlights the importance of understanding a variety of effects on the characteristics of the ABL during an HW and DWs. Thus, knowledge of the ABL conditions associated with DWs during an HW may be useful for predicting local to regional extreme temperature events. Additional studies involving high-resolution numerical simulations and observation campaigns are necessary to investigate the contributions of rotors, hydraulic jumps, gravity-wave breaking, and the effects caused by adiabatic processes in increasing warming and drying of the ABL.

Author Contributions: Conceptualization, M.S., C.E.d.R. and G.A.D.; methodology, M.S., C.E.d.R., N.C.S.d.R. and C.B.; software, M.S., C.E.d.R., N.C.S.d.R., D.S.F. and C.B.; validation, M.S. and C.E.d.R.; formal analysis, M.S., C.E.d.R., D.L.H., S.E.T.F., N.T.B. and G.A.D.; investigation, M.S., C.E.d.R. and G.A.D.; data curation, M.S., C.E.d.R., N.C.S.d.R., D.S.F., D.R.R. and C.B. writing—original draft preparation, M.S., C.E.d.R., D.L.H., S.E.T.F., N.T.B., O.A., D.R.R. and G.A.D.; writing—review and

editing, all authors; visualization, M.S., C.E.d.R., D.S.F. and C.B.; project administration, G.A.D.; funding acquisition, T.T., D.R.R. and G.A.D. All authors have read and agreed to the published version of the manuscript.

Institutional Review Board Statement: Not applicable.

Informed Consent Statement: Not applicable.

Data Availability Statement: The data used in this study are available by contacting the corresponding author.

Conflicts of Interest: The authors declare no conflict of interest.

Abbreviations

The following abbreviations are used in this manuscript:

ABL	Atmospheric Boundary Layer
CPC	Climate Prediction Center
DW	Downslope winds
HW	Heat Wave
LST	Local standard time
RS	Rio Grande do Sul
SM	Santa Maria
UFSM	Federal University of Santa Maria

References

1. Garratt, J.R. *The Atmospheric Boundary Layer*; Cambridge University Press: Cambridge, UK, 1992; Volume 416, p. 444.
2. Grisogono, B.; Belušić, D. A review of recent advances in understanding the mesoand microscale properties of the severe Bora wind. *Tellus A Dyn. Meteorol. Oceanogr.* **2009**, *61*, 1–16. [CrossRef]
3. Babić, N.; Večenaj, Ž.; Kozmar, H.; Horvath, K.; De Wekker, S.F.; Grisogono, B. On turbulent fluxes during strong winter bora wind events. *Bound.-Layer Meteorol.* **2016**, *158*, 331–350. [CrossRef]
4. Smith, R.B. 100 Years of Progress on Mountain Meteorology Research. *Meteorol. Monogr.* **2019**, *59*, 20–21. [CrossRef]
5. Arrillaga Mitxelena, J.A.; Yagüe Anguis, C.; Román Cascón, C.; Sastre Marugán, M.; Jiménez, M.A.; Maqueda Burgos, G.; Vilà-Guerau de Arellano, J. From weak to intense downslope winds: Origin, interaction with boundary-layer turbulence and impact on CO2 variability. *Atmos. Chem. Phys.* **2019**, *19*, 4615–4635. [CrossRef]
6. Stefanello, M.; de Lima Nascimento, E.; da Rosa, C.E.; Degrazia, G.; Mortarini, L.; Cava, D. A Micrometeorological Analysis of the Vento Norte Phenomenon in Southern Brazil. *Bound.-Layer Meteorol.* **2020**, *176*, 415–439. [CrossRef]
7. da Rosa, C.E.; Stefanello, M.; Maldaner, S.; Facco, D.S.; Roberti, D.R.; Tirabassi, T.; Degrazia, G.A. Employing Spectral Analysis to Obtain Dispersion Parameters in an Atmospheric Environment Driven by a Mesoscale Downslope Windstorm. *Int. J. Environ. Res. Public Health* **2021**, *18*, 13027. [CrossRef]
8. da Rosa, C.E.; Stefanello, M.; de Lima Nascimento, E.; Rossi, F.D.; Roberti, D.R.; Degrazia, G.A. Meteorological observations of the Vento Norte phenomenon in the central region of Rio Grande do Sul. *Rev. Bras. Meteorol.* **2021**, *36*, 367–376. [CrossRef]
9. Večenaj, Ž.; Malečić, B.; Grisogono, B. Estimation of Turbulent Triplet Covariances for Bora Flows. *Fluids* **2021**, *6*, 452. [CrossRef]
10. Abatzoglou, J.T.; Hatchett, B.J.; Fox-Hughes, P.; Gershunov, A.; Nauslar, N.J. Global climatology of synoptically-forced downslope winds. *Int. J. Climatol.* **2021**, *41*, 31–50. [CrossRef]
11. Wang, W.; Zhou, W.; Li, X.; Wang, X.; Wang, D. Synoptic-scale characteristics and atmospheric controls of summer heat waves in China. *Clim. Dyn.* **2016**, *46*, 2923–2941. [CrossRef]
12. Nishi, A.; Kusaka, H. Effect of foehn wind on record-breaking high temperature event (41.1 °C) at Kumagaya on 23 July 2018. *Sola* **2019**, *15*, 17–21. [CrossRef]
13. da Rosa, C.E.; Stefanello, M.; dos Reis Facco, N.C.S.; Stefanello, D.; Ferraz, S.T.; Boiaski, N.T.; Herdies, D.; Degrazia, G.A. Winter heat waves characteristics associated with downslope windstorm in south Brazil. *Int. J. Climatol.* **2023**, *submitted*.
14. Smith, C.; Hatchett, B.J.; Kaplan, M. A surface observation based climatology of Diablo-like winds in California's Wine Country and western Sierra Nevada. *Fire* **2018**, *1*, 25. [CrossRef]

15. Schwarz, L.; Malig, B.; Guzman-Morales, J.; Guirguis, K.; Ilango, S.D.; Sheridan, P.; Gershunov, A.; Basu, R.; Benmarhnia, T. The health burden fall, winter and spring extreme heat events in the in Southern California and contribution of Santa Ana Winds. *Environ. Res. Lett.* **2020**, *15*, 054017. [CrossRef]

16. Chow, F.K.; De Wekker, S.F.; Snyder, B.J. *Mountain Weather Research and Forecasting: Recent Progress and Current Challenges*; Springer: Berlin/Heidelberg, Germany, 2013; Volume 750.

17. Elvidge, A.D.; Renfrew, I.A. The causes of foehn warming in the lee of mountains. *Bull. Am. Meteorol. Soc.* **2016**, *97*, 455–466. [CrossRef]

18. da Rosa, C.E.; Stefanello, M.; Facco, D.S.; Roberti, D.R.; Rossi, F.D.; Nascimento, E.d.L.; Degrazia, G.A. Regional-scale meteorological characteristics of the Vento Norte phenomenon observed in Southern Brazil. *Environ. Fluid Mech.* **2022**, 22, 819–837. [CrossRef]

19. Durran, D.R. Mountain waves and downslope winds. In *Atmospheric Processes over Complex Terrain*; Springer: Berlin/Heidelberg, Germany, 1990; pp. 59–81.

20. Strauss, L.; Serafin, S.; Haimov, S.; Grubišić, V. Turbulence in breaking mountain waves and atmospheric rotors estimated from airborne in situ and Doppler radar measurements. *Q. J. R. Meteorol. Soc.* **2015**, *141*, 3207–3225. [CrossRef]

21. Durran, D. MOUNTAIN METEOROLOGY | Downslope Winds. In *Encyclopedia of Atmospheric Sciences*, 2nd ed.; North, G.R., Pyle, J., Zhang, F., Eds.; Academic Press: Oxford, UK, 2015; pp. 69–74. [CrossRef]

22. Carvalho, L.; Duine, G.J.; Jones, C.; Zigner, K.; Clements, C.; Kane, H.; Gore, C.; Bell, G.; Gamelin, B.; Gomberg, D.; et al. The sundowner winds experiment (SWEX) pilot study: Understanding downslope windstorms in the Santa Ynez Mountains, Santa Barbara, California. *Mon. Weather Rev.* **2020**, *148*, 1519–1539. [CrossRef]

23. Duine, G.J.; Jones, C.; Carvalho, L.M.; Fovell, R.G. Simulating Sundowner winds in coastal Santa Barbara: Model validation and sensitivity. *Atmosphere* **2019**, *10*, 155. [CrossRef]

24. Xue, H.; Giorgetta, M.A. A large-eddy simulation study on the diurnally evolving nonlinear trapped lee waves over a two-dimensional steep mountain. *J. Atmos. Sci.* **2021**, *78*, 399–415. [CrossRef]

25. Bozkurt, D.; Rojas, M.; Boisier, J.P.; Rondanelli, R.; Garreaud, R.; Gallardo, L. Dynamical downscaling over the complex terrain of southwest South America: Present climate conditions and added value analysis. *Clim. Dyn.* **2019**, *53*, 6745–6767. [CrossRef]

26. Demortier, A.; Bozkurt, D.; Jacques-Coper, M. Identifying key driving mechanisms of heat waves in central Chile. *Clim. Dyn.* **2021**, *57*, 2415–2432. [CrossRef]

27. Turner, J.; Lu, H.; King, J.C.; Carpentier, S.; Lazzara, M.; Phillips, T.; Wille, J. An extreme high temperature event in coastal East Antarctica associated with an atmospheric river and record summer downslope winds. *Geophys. Res. Lett.* **2022**, *49*, e2021GL097108. [CrossRef]

28. Duine, G.J.; Carvalho, L.M.; Jones, C. Mesoscale patterns associated with two distinct heatwave events in coastal Santa Barbara, California, and their impact on local fire risk conditions. *Weather Clim. Extrem.* **2022**, *37*, 100482. [CrossRef]

29. Robinson, P.J. On the definition of a heat wave. *J. Appl. Meteorol. Climatol.* **2001**, *40*, 762–775. [CrossRef]

30. Michelozzi, P.; De'Donato, F.; Accetta, G.; Forastiere, F.; d'Ovidio, M.; Perucci, C.; Kalkstein, L. Impact of heat waves on mortality-Rome, Italy, June-August 2003 (Reprinted from MMWR, vol 53, pg 369–371, 2004). *JAMA-J. Am. Med Assoc.* **2004**, *291*, 2537–2538.

31. Ghobadi, A.; Khosravi, M.; Tavousi, T. Surveying of heat waves impact on the urban heat islands: Case study, the Karaj City in Iran. *Urban Clim.* **2018**, *24*, 600–615.

32. dos Reis, N.C.S.; Boiaski, N.T.; Ferraz, S.E.T. Characterization and spatial coverage of heat waves in subtropical Brazil. *Atmosphere* **2019**, *10*, 284. [CrossRef]

33. Marengo, J.A.; Ambrizzi, T.; Barreto, N.; Cunha, A.P.; Ramos, A.M.; Skansi, M.; Molina Carpio, J.; Salinas, R. The heat wave of October 2020 in central South America. *Int. J. Climatol.* **2021**, *42*, 2281–2298.

34. Garcia de Araújo, G.R.; Frassoni, A.; Sapucci, L.F.; Bitencourt, D.; de Brito Neto, F.A. Climatology of heatwaves in South America identified through ERA5 reanalysis data. *Int. J. Climatol.* **2022**. [CrossRef]

35. Pezza, A.B.; Van Rensch, P.; Cai, W. Severe heat waves in Southern Australia: Synoptic climatology and large scale connections. *Clim. Dyn.* **2012**, *38*, 209–224. [CrossRef]

36. Geirinhas, J.L.; Trigo, R.M.; Libonati, R.; Coelho, C.A.; Palmeira, A.C. Climatic and synoptic characterization of heat waves in Brazil. *Int. J. Climatol.* **2018**, *38*, 1760–1776. [CrossRef]

37. Zhang, Y.; Wang, L.; Santanello, J.A., Jr.; Pan, Z.; Gao, Z.; Li, D. Aircraft observed diurnal variations of the planetary boundary layer under heat waves. *Atmos. Res.* **2020**, *235*, 104801. [CrossRef]

38. An, N.; Zuo, Z. Investigating the influence of synoptic circulation patterns on regional dry and moist heat waves in North China. *Clim. Dyn.* **2021**, *57*, 1227–1240. [CrossRef]

39. Miralles, D.G.; Teuling, A.J.; Van Heerwaarden, C.C.; Vilà-Guerau de Arellano, J. Mega-heatwave temperatures due to combined soil desiccation and atmospheric heat accumulation. *Nat. Geosci.* **2014**, *7*, 345–349. [CrossRef]

40. Horton, R.M.; Mankin, J.S.; Lesk, C.; Coffel, E.; Raymond, C. A review of recent advances in research on extreme heat events. *Curr. Clim. Chang. Rep.* **2016**, *2*, 242–259. [CrossRef]

41. Ruthrof, K.X.; Breshears, D.D.; Fontaine, J.B.; Froend, R.H.; Matusick, G.; Kala, J.; Miller, B.P.; Mitchell, P.J.; Wilson, S.K.; van Keulen, M.; et al. Subcontinental heat wave triggers terrestrial and marine, multi-taxa responses. *Sci. Rep.* **2018**, *8*, 13094. [CrossRef]

42. Thompson, R.; Hornigold, R.; Page, L.; Waite, T. Associations between high ambient temperatures and heat waves with mental health outcomes: A systematic review. *Public Health* **2018**, *161*, 171–191. [CrossRef]

43. Breshears, D.D.; Fontaine, J.B.; Ruthrof, K.X.; Field, J.P.; Feng, X.; Burger, J.R.; Law, D.J.; Kala, J.; Hardy, G.E.S.J. Underappreciated plant vulnerabilities to heat waves. *New Phytol.* **2021**, *231*, 32–39. [CrossRef]

44. He, B.J.; Wang, J.; Liu, H.; Ulpiani, G. Localized synergies between heat waves and urban heat islands: Implications on human thermal comfort and urban heat management. *Environ. Res.* **2021**, *193*, 110584. [CrossRef]

45. Arias, P.; Bellouin, N.; Coppola, E.; Jones, R.; Krinner, G.; Marotzke, J.; Naik, V.; Palmer, M.; Plattner, G.K.; Rogelj, J.; et al. Climate Change 2021: The Physical Science Basis. Contribution of Working Group14 I to the Sixth Assessment Report of the Intergovernmental Panel on Climate Change. Technical Summary 2021. Available online: https://elib.dlr.de/137584/ (accessed on 10 July 2022).

46. Marengo, J.A.; Camargo, C.C. Surface air temperature trends in Southern Brazil for 1960–2002. *Int. J. Climatol.* **2008**, *28*, 893–904. [CrossRef]

47. Ceccherini, G.; Russo, S.; Ameztoy, I.; Romero, C.P.; Carmona-Moreno, C. Magnitude and frequency of heat and cold waves in recent decades: The case of South America. *Nat. Hazards Earth Syst. Sci.* **2016**, *16*, 821–831. [CrossRef]

48. Bitencourt, D.P.; Fuentes, M.V.; Franke, A.E.; Silveira, R.B.; Alves, M.P. The climatology of cold and heat waves in Brazil from 1961 to 2016. *Int. J. Climatol.* **2020**, *40*, 2464–2478. [CrossRef]

49. Kottek, M.; Grieser, J.; Beck, C.; Rudolf, B.; Rubel, F. World map of the Köppen-Geiger climate classification updated. *Meteorol. Z.* **2006**, *15*, 259–263. [CrossRef]

50. Peel, M.C.; Finlayson, B.L.; McMahon, T.A. Updated world map of the Köppen-Geiger climate classification. *Hydrol. Earth Syst. Sci.* **2007**, *11*, 1633–1644. [CrossRef]

51. Hersbach, H.; Bell, B.; Berrisford, P.; Horányi, A.; Sabater, J.M.; Nicolas, J.; Radu, R.; Schepers, D.; Simmons, A.; Soci, C.; et al. Global reanalysis: Goodbye ERA-Interim, hello ERA5. *ECMWF Newsl.* **2019**, *159*, 17–24.

52. Hersbach, H.; Bell, B.; Berrisford, P.; Hirahara, S.; Horányi, A.; Muñoz-Sabater, J.; Nicolas, J.; Peubey, C.; Radu, R.; Schepers, D.; et al. The ERA5 global reanalysis. *Q. J. R. Meteorol. Soc.* **2020**, *146*, 1999–2049. [CrossRef]

53. Do Meio Ambiente e Insfraestrutura do Rio Grande do Sul SEMA, S. Estiagem 2020/2021/2022. Available online: https://sema.rs.gov.br/estiagem-rs (accessed on 18 October 2022).

54. INMET NOTA METEOROLÓGICA 14/01/2022: Onda de Calor Atinge seu Auge e máXimas Passam dos 40 °C no Rio Grande do Sul. Technical Report, Brazilian National Institute of Meteorology INMET. Available online: https://portal.inmet.gov.br/notasTecnicas (accessed on 18 October 2022).

55. INMET NOTA METEOROLÓGICA 17/01/2022: Onda de Calor Bate Novos Recordes e Temperatura Alcança os 41.8 °C no Rio Grande do Sul. Technical Report, Brazilian National Institute of Meteorology INMET. Available online: https://portal.inmet.gov.br/notasTecnicas (accessed on 18 October 2022).

56. INMET NOTA METEOROLÓGICA 20/01/2022: Onda de Calor Persiste no Estado do Rio Grande do Sul. Technical Report, Brazilian National Institute of Meteorology INMET. Available online: https://portal.inmet.gov.br/notasTecnicas (accessed on 18 October 2022).

57. Alvarez, M.S.; Cerne, B.; Osman, M.; Vera, C.S. Intraseasonal and low frequency processes contributing to the December 2013 heat wave in Southern South America. *Clim. Dyn.* **2019**, *53*, 4977–4988. [CrossRef]

58. Sun, X.; Cook, K.H.; Vizy, E.K. The South Atlantic subtropical high: Climatology and interannual variability. *J. Clim.* **2017**, *30*, 3279–3296. [CrossRef]

59. Zigner, K.; Carvalho, L.M.; Jones, C.; Duine, G.J. Extreme winds and fire weather in coastal Santa Barbara County, CA: An observational analysis. *Int. J. Climatol.* **2022**, *42*, 597–618. [CrossRef]

60. Degrazia, G.A.; Rizza, U.; Stefanello, M.; Maldaner, S.; Roberti, D.R.; Martins, L.G.N.; Anabor, V.; Puhales, F.S.; Dal Piva, E.; Acevedo, O.C.; et al. An overview of the micrometeorological field campaign at Santa Maria, Southern Brazil: The Pampa-2016 experiment. *Meteorol. Appl.* **2018**, *25*, 435–444. [CrossRef]

61. André, J.; Mahrt, L. The nocturnal surface inversion and influence of clear-air radiative cooling. *J. Atmos. Sci.* **1982**, *39*, 864–878. [CrossRef]

62. Vera, C.; Baez, J.; Douglas, M.; Emmanuel, C.; Marengo, J.; Meitin, J.; Nicolini, M.; Nogues-Paegle, J.; Paegle, J.; Penalba, O.; et al. The South American low-level jet experiment. *Bull. Am. Meteorol. Soc.* **2006**, *87*, 63–78. [CrossRef]

63. Andreas, E.L.; Claffy, K.J.; Makshtas, A.P. Low-level atmospheric jets and inversions over the western Weddell Sea. *Bound.-Layer Meteorol.* **2000**, *97*, 459–486. [CrossRef]